Measured and simulated performance of a ceramic micro-mechanical beam steering device at 94 GHz

T. D. Drysdale, E. D. Walsby, and D. R. S. Cumming*

Department of Electronics and Electrical Engineering, University of Glasgow

Rankine Building, Oakfield Avenue, Glasgow G12 8LT, United Kingdom

**Corresponding author: d.cumming@elec.gla.ac.uk*

We report the first experimental demonstration of a transmission mode micro-mechanical beam steering device for use in stand-off terahertz imaging and spectroscopy. The device was constructed by laminating laser-cut 96% alumina sheets to form two plates with interlocking rectangular gratings of 762 μm period and characterised at 94 GHz in a free-space measurement set-up with an automated elevation scan. Plate tilts of up to 6^o, deflected the transmitted beam by 6^o for the transverse electric (TE) polarisation, and 4^o for the transverse magnetic polarisation. Finite difference time domain simulations of the TE performance were in good agreement with the measurements.

OCIS codes: 120.5060 Phase modulation 230.3990 Microstructure devices, 260.1440 Birefringence, 350.4010 Microwaves

Terahertz source and detector technology continues to develop at a rapid pace, enabling an ever-wider range of applications. Early systems emitted and detected broad-band pulses using ultrafast lasers and photo-conductive switches [1] or non-linear crystals [2] and had the disadvantage of being bulky and expensive. The development of quasi-monochromatic continuous wave systems based on the photo-mixing of two diode laser sources of dissimilar wavelength [3] has demonstrated the potential for compact, inexpensive terahertz systems. Further size reductions are likely to come from solid-state approaches such as quantum cascade lasers [4]. In order to fully exploit such technology at the system level, it is necessary to have full control over the emitted quasi-optical beams. An important application is that of beam steering, with a requirement to image a 1m target at 10m (implying a beam steering through $\pm 2.8^{o}$) [5]. Phased array techniques typically used at microwave frequencies [6]. Unfortunately they are impractical for use at terahertz frequencies since the required precision in the control of phase is unattainable. This difficulty is avoided in optics by the use of micro-electro-mechanical systems (MEMS) devices, such as reflection-mode spatial modulators [7] based on arrays of micro-actuated mirrors. Similar benefits are expected to accrue to present and future terahertz systems through using MEMS devices, with the further advantage of being able to make even more compact transmission mode devices due to the low loss at terahertz frequencies of typical micromachining substrates.

A number of terahertz micromechanical devices have been demonstrated already, including fixed Fresnel lenses [8] and variable polarisation compensators [9]. Tuneable filters have been successfully applied to a commercial terahertz system [3]. As stand-off distances increase, the ability to compactly steer a beam without shifting the delicately-aligned generation or detection optics becomes important. For example, two-axis scanning mirrors are acceptable

for image formation in a lab-based contact-imaging system but may be inappropriate for future non-contact imaging systems that may be used in the field. We recently proposed a solution to this problem in the form of a transmission-mode beam steering device based on an interlocking artificial dielectric [10] that can be microfabricated in silicon or any other readily-machinable low-loss, low-dispersion dielectric material. In this Letter, we report the first experimental demonstration of such a device. Due to the relatively recent development of metamaterial based devices for terahertz quasi-optics, the characterization of micromechanical implementations is an important step towards the ultimate goal of achieving MEMS devices with integrated electro-mechanical actuators.

The beam steering device comprises two plates with interlocking rectangular gratings, as shown in Fig. 1. The gratings are chosen to have subwavelength period Λ, and groove depth d on the order of a wavelength. The tilt angle θ_t is 0^o when the plates are parallel and fully interlocked. By tilting one plate such that the plates are fully interlocked at one end and partially interlocked at the other, a graded phase delay medium is created. The greater θ_t, the greater the increase in phase delay from one side of the device to the other, thus the greater the normally incident beam is deflected, or steered, θ_s, upon transmission. The transverse electric (TE) and transverse magnetic (TM) linear polarisations are defined with respect to the grating vector $\boldsymbol{k}$. The TE electric field (E_{TE}) is perpendicular to $\boldsymbol{k}$, while the TM electric field (E_{TM}) is parallel to $\boldsymbol{k}$. TE polarisations experience a positive steer ($\theta_s > 0$) whilst TM polarisations experience a negative steer ($\theta_s < 0$), due to the birefringence of the rectangular gratings.

A detailed quasi-analytical and numerical analysis of the performance can be found in [10], including the discrete array factor (AF) calculation. The AF calculation provides the insight of a simple analytical model but allows for improved accuracy through the incorporation

of simple numerical techniques. Summarising the method briefly, we consider the discretised, angular distribution of the transmission coefficient of the device, *T(θ):*

$$T(\theta) = \frac{1}{N}\sum_{m=1}^{N} A(m)\mathrm{e}^{\mathrm{j}(k_0 m\Delta z\cos\theta+\alpha(m)+\beta(z))}$$

where N is the number of points modelled across the device, Δz is the distance between the m^{th} and $m+1^{th}$ points, k_0 is the propagation constant in air, *A(m)* is the magnitude and $\alpha(m)$ the phase of the transmission coefficient for the m^{th} section of the device and $\beta(x)$ is a phase correction factor to account for the wedge shape of the device. The transmission coefficient is calculated separately for each of the *m* sections of the device, using second order effective medium theory to homogenise the gratings and a 1-dimensional T-matrix method account for multiple internal reflections [10].

A prototype device was constructed from laser cut sections of 381 μm thick ceramic. By laminating together sections of alternating size (4 × 33 mm, and 8 × 33 mm), a device of 33 mm by 33 mm was produced with b = 4 mm, d = 4 mm and Λ = 762 μm. The laminations in the plates were semi-permanently glued by allowing a thin cyano-acrylate adhesive to wick into the joints. In order to ensure that the plates could be fully interlocked in this, the bottom plate was assembled and glued in a specially made plastic clamp, then the top plate was assembled using the bottom plate as a guide. The plastic clamp was removed for the experiment. For mass production, we envisage the use of moulds to directly create plates using either powdered alumina or high-refractive index plastics. For the batch fabrication of devices designed to operate at higher frequencies, e.g. 1 THz, it would be more appropriate to use conventional bulk micromachining techniques [11]. The tilt angle between the plates was adjusted manually.

The experimental setup is shown in Fig. 2. It comprised a Gunn diode oscillator producing 0 dBm of power at 94 GHz into a standard gain WR-10 pyramidal horn antenna with the boresight oriented vertically. The source and transmitting horn were enclosed in absorbing foam, except for an aperture above the transmitting horn. A correctly aligned aperture eliminated stray fields and did not significantly alter the transmitted beam pattern, whereas deliberate misalignment resulted in an asymmetrical beam pattern. Fan-forced air cooling was used to avoid thermal drift of the oscillator's output frequency and power. Due the narrow-band operation of the available source, we only show results for a single frequency.

The device was mounted over a mechanically stable absorbing foam aperture on the axis of rotation of a motorised rotation stage. A second horn antenna was mounted on a foam-covered metal arm attached to rotation stage, at a radius of 20 cm, to allow automated elevation scans. A commercially available laser level tool was used to check and carefully adjust the alignment of the system. An Agilent 8564E spectrum analyser with an external diplexer and harmonic mixer (conversion loss 30 dB) was used to record the magnitude of the transmitted beam. Both the rotation stage and spectrum analyser were computer controlled, allowing automated capture of the radiation pattern. For each device setting in the range $0° \le \theta_t \le 6°$, the radiation pattern was recorded between $-45°$ and $+45°$ in $0.5°$ steps. Measurements were conducted for the TE polarisation first, then for the TM polarisation.

Since the material and dimensions of the device were different to the example in [10], simulations were performed with a rigorous full vector electromagnetic solver tool using the finite-difference time-domain (FDTD) algorithm [12]. The 3-dimensional simulation domain

comprised 120 × 490 × 460 ($x \times y \times z$) cubic mesh cells of side length 40 μm, with an additional 10 layers of perfectly matched layer (PML) boundary conditions. See Fig. 1(a) for the orientation of the FDTD simulation axes relative to the device. Five periods of the device (3.8 mm) were modelled in the x direction and 16 mm in the z direction. For TE polarisation, a single E_z field component located opposite the middle of the fixed plate but 10 cells away from the device was stimulated. The dipole nature of this type of source gives a rotationally invariant pattern in the TM polarisation so simulation results are only presented for TE polarisation. Using continuous wave excitation at 94 GHz with a raised sine envelope, each simulation was run until convergence (typically 160,000 time steps). Far field patterns were calculated using the steady state field patterns recorded in the last period of the simulation, 6 cells inside the PML boundary.

Examples of the measured TE and TM radiation patterns are shown in Fig. 3, for the case of the maximum 6^o tilt. The magnitude of the two radiation patterns has been normalised to aid comparison. The TE pattern steers by $6°$ while the TM pattern steers by $4°$ in the opposite direction. The TE pattern shows the steered E-plane radiation pattern of the horn antenna, hence it has a narrower main lobe but more prominent side lobes compared to the TM (H-plane) pattern. The difference in the E-plane and H-plane radiation pattern of the horn antenna is a consequence of the dimensions of the horn's aperture and not related to the device performance [13].

The measured tilt-steer performance of the device is plotted in Fig. 4 for TE and TM polarisations, along with the simulated TE tilt-steer performance and the results of the discrete array factor calculations. While the measured data points are indicated by symbols, lines have

been added to guide the reader. We estimate the error in the measurement to be ±1°. The mid point of the measured radiation patterns was determined by calculating the centre point of a curve fitted between the -3dB points of the main lobe. While we show single scans in Fig. 3, we calculated the centre point using data averaged across several scans taken in each carefully measured positional setting. This averaging helped further reduce the noise floor of the measurement, but did not compensate for any slight error in the device's positional setting. The discrete array factor (AF) calculations were performed after the experiment, using the aperture size and fill factor as fitting parameters. The AF results plotted in Fig. 4 used a 16 mm aperture in the centre of the device and a fill factor of 0.517. The fill factor implies that the longer teeth were constructed from alumina sheets that were, on average, 3.5% thicker than the nominal value, and the shorter teeth from sheets that were 3.5% thinner. This is plausible because the manufacturer's data sheet indicates the sheet thickness tolerance is ±7%.

The TM steer shows a near linear dependence upon tilt as would be expected by comparison to the results in [10], whereas the TE steer is greater, but less linear. The AF calculation shown in Fig. 4 exaggerates the non-linearity in the TM performance because it only accounts for internal reflections that are parallel to the direction of propagation of the incident wave and has reduced accuracy when the magnitude of the internal reflections is increased by omitting the anti-reflection coatings. The slight 'opposite steer' for both TE and TM arising at a tilt of 1° is a measurement artifact arising from error in adjusting the tilt of the device to such a small angle. The local maximum for TE and TM at a tilt of 2° is a consequence of multiple internal reflections between the tilted inner faces of the device. The simulated performance for TE agrees reasonably well with the measured data. The presence of the non-linearity at 2° in the

simulated data confirms that this is not a measurement error. In order to obtain maximum steering performance in an application using the TE polarisation, the effect of any non-linearity could be mitigated with an appropriate control algorithm.

In conclusion, we present the first experimental realisation of a beam steering device for use at millimetre wave and terahertz frequencies. The device was constructed from laminated laser cut ceramic sheets, and the beam steering performance characterised in a computer-controlled setup at 94 GHz. The plate tilt was controlled by hand. As expected, the steering performance differed for TE and TM polarisations. The TE polarisation steering up to $6°$ for a relative plate tilt of $6°$, whereas for the same tilt the TM polarisation steered less, at 4^{o}, and in the opposite direction. Such a device can be configured to give deflections over a working range of 12^{o} by orienting for the TE polarisation and tilting the plates in both directions, i.e. $-6° \le \theta_t \le 6°$. These deflections exceed the already identified performance requirement of $\pm 2.8^{o}$ deflection that is required to image a 1 m target area that is 10 m distant [5].

References

1. D. H. Austen, K. P. Cheung, and P. R. Smith, “Picosecond photoconducting Hertzian dipoles,” Appl. Phys. Lett. **45**, 284 - 286 (1984)
2. K. H. Yang, P. L. Richards and Y. R. Shen, “Generation of far-infrared radiation by picosecond light pulses in LiNbO3," Appl. Phys. Lett. **19**, 320 - 323 (1971)
3. I. S. Gregory, W. R. Tribe, M. J. Evans, T. D. Drysdale, D. R. S. Cumming, M. Missous, “Multi-channel homodyne detection of continuous-wave terahertz radiation,” Appl. Phys. Lett. **87**, 034106 (2005)
4. B.S. Williams, S. Kumar, H. Callebaut, Q. Hu, J. L. Reno, Electron. Lett. “3.4 THz quantum cascade laser operating above liquid nitrogen temperature,” **39**, 915 (2003)
5. K. J. Linden, W.R. Neal, J. Waldman, A. J. Gatesman, A. Danylov, "Terahertz laser based standoff imaging system," *Applied Imagery and Pattern Recognition Workshop, 2005. Proceedings. 34th* , pp 8 - 15, 19-21 Oct. 2005
6. L. Brennan, “Angular accuracy of a phased array radar,” IEEE Tran. Antennas Prop. **9**, 268 (1961)
7. T. S. Kim, S. S. Lee, Y. Yee, J. U. Bu, C. G. Park, M. H. Ha, “Large tilt angle electrostatic force actuated micro-mirror ,” IEEE Photon. Technol .Lett **14**, 1569 (2002)
8. E. D. Walsby, R. Cheung, R. J. Blaikie, D. R. S. Cumming, “Fabrication of multilevel silicon diffractive lenses for terahertz frequencies,” Proc. SPIE 3879 **79** (1999)
9. T. D. Drysdale, R. J. Blaikie, H. M. H. Chong, D. R. S. Cumming, “Artificial Dielectric Devices for variable polarization compensation at millimeter and submillimeter wavelengths,” IEEE Trans. Antennas Prop. **51** 3072 (2003)

10. D. R. S. Cumming, T. D. Drysdale, “A micro-mechanical beam-steering device for terahertz frequencies,” Opt. Commun. **259**, 373 (2006)
11. T. D. Drysdale, G. Mills, S. M. Ferguson, R. J. Blaikie, D. R. S. Cumming, “Terahertz tuneable filters made by self-releasing deep dry etch process,” Microelectronic Engineering **73 - 74**, 441 (2004)
12. XFDTD, Remcom Inc., State College, PA 16801
13. C. A. Balanis, “Antenna theory analysis and design,” John Wiley & Sons, Inc., Singapore, 1982

Figure Captions

Fig. 1. Diagram of a section of the beam steering device: (a) side view, (b) front view (not to scale).

Fig. 2. Diagram of the experimental setup, comprising an absorbing foam aperture upon which the beamsteering device is placed, a Gunn diode continuous wave source of 94 GHz illumination under the aperture and a receiving horn on a rotation stage above the aperture. The axis of rotation of the receiving horn is located at the centre of the beamsteering device.

Fig. 3. Lobe pattern of TM and TE with a 6° plate tilt.

Fig. 4. Steering performance of the measured device as a function of relative plate tilt. Finite difference time domain (FDTD) simulation results are shown for the TE polarisation, while discrete array factor (AF) calculation results are shown for both polarisations.

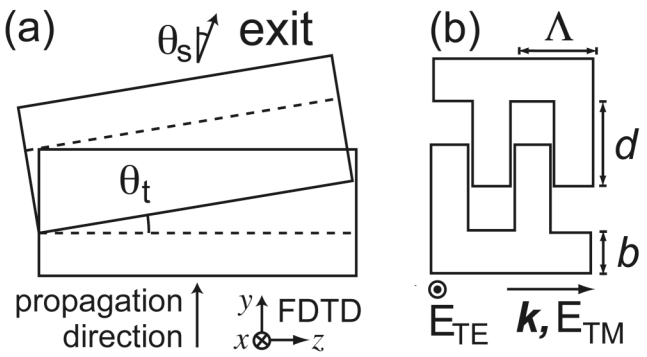

Fig. 1

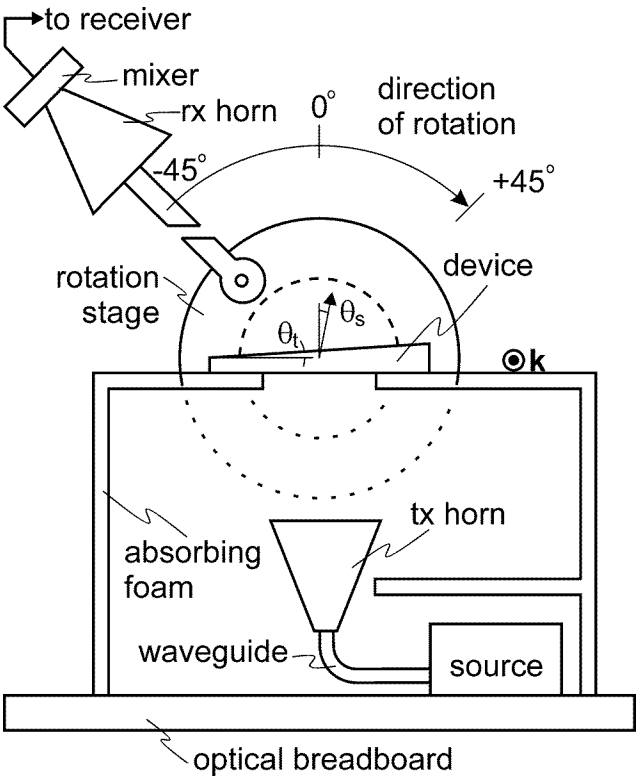
to receiver
mixer
rx horn
0°
direction
of rotation
-45°
+45°
rotation
stage
device
θs
θt
k
tx horn
absorbing
foam
waveguide
source
optical breadboard

Fig. 2

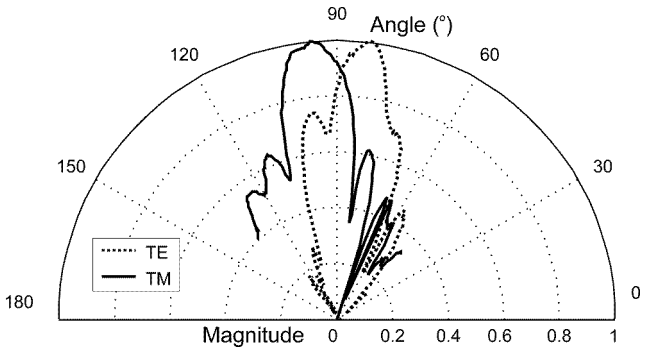

Fig. 3

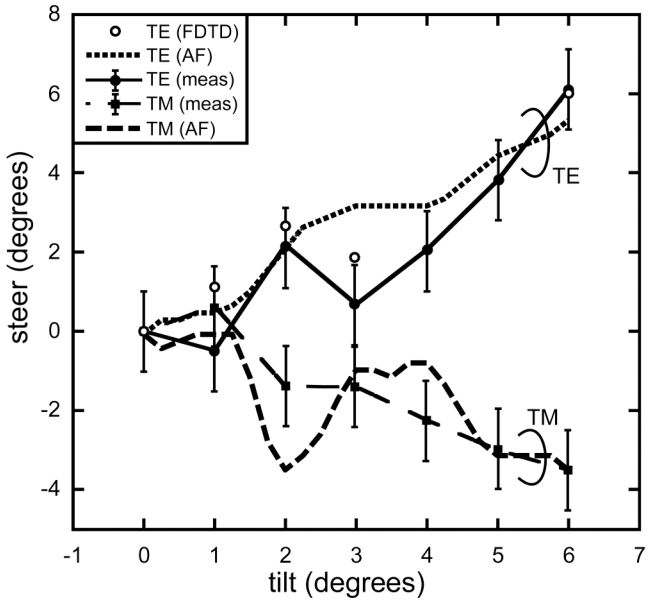
TE (FDTD)
TE (AF)
TE (meas)
TM (meas)
TM (AF)
steer (degrees)
tilt (degrees)
TE
TM
8
6
4
2
0
-2
-4
-1
0
1
2
3
4
5
6
7

Fig. 4